Chemical Engineering Journal 395 (2020) 124979

Contents lists available at ScienceDirect

Chemical Engineering Journal

journal homepage: www.elsevier.com/locate/cej

Short communication

A robust electrospun separator modified with *in situ* grown metal-organic frameworks for lithium-sulfur batteries

Cheng Zhou[a], Qiu He[b], Zhaohuai Li[a], Jiashen Meng[a], Xufeng Hong[a], Yan Li[b], Yan Zhao[b], Xu Xu[a,*], Liqiang Mai[a,*]

[a] State Key Laboratory of Advanced Technology for Materials Synthesis and Processing, International School of Materials Science and Engineering, Wuhan University of Technology, Wuhan 430070, Hubei, China
[b] State Key Laboratory of Silicate Materials for Architectures, International School of Materials Science and Engineering, Wuhan University of Technology, Wuhan 430070, Hubei, China

HIGHLIGHTS

- The PAN membrane was *in situ* modified with MOF by LPCVD as the separator.
- This separator can effectively trap polysulfides and protect the lithium anode.
- The Li-S battery delivered a long lifespan of 600 cycles at 5 C.
- A high capacity of 7.8 mAh cm^{-2} was obtained with sulfur loading of 7.7 mg cm^{-2}.

ARTICLE INFO

Keywords:
Novel separator
Metal-organic framework
Low pressure chemical vapor deposition
Shuttle effect
Lithium-sulfur batteries

ABSTRACT

Because of the existence of the soluble lithium polysulfides, the requirement for an ideal separator for lithium sulfur (Li-S) batteries is higher than that in LIBs. Herein, we report a double-layered MOF-PAN/rGO-PAN nanofiber membrane as an alternative to commercial polyolefin separators for Li-S battery. This PAN-based membrane possesses the intrinsic advantages of good mechanical property, thermal stability and high electrolyte uptake, showing a high lithium ion transference number of 0.81. The *in situ* grown MOF particles by low pressure chemical vapor deposition attach on the surface of the nanofibers tightly, and these exposed particles can maximize the utilization for trapping polysulfides through chemisorption. With this novel functional separator, the Li-S batteries can provide a high initial capacity of 1302 mAh g^{-1} at 0.5 C. At a high rate of 5 C, the capacity decay rate is only 0.03% per cycle over 600 cycles. More importantly, even with a high sulfur loading of 7.7 mg cm^{-2}, the Li-S battery is able to deliver a high areal capacity of 7.8 mAh cm^{-2} after 50 cycles.

1. Introduction

With the shortage of earth resources and environmental pollution, higher requirements have been put forward for energy storage devices [1,2]. Traditional Li-ion batteries (LIBs) have been developed rapidly, however, the energy density of LIBs is still far below the ever increasing requirement. With the earth abundant resource sulfur as the cathode materials, lithium-sulfur (Li-S) battery possesses a theoretical capacity of 1675 mAh g^{-1} and an energy density of 2600 Wh kg^{-1}, which has attracted widespread attentions [3,4]. However, the practical application of Li-S battery is impeded by the rapid capacity fading, which is caused by several key factors [5,6], including the shuttling effect of the soluble polysulfides, the insulating properties of sulfur and Li_2S, and the considerable structural variation of the cathode during the cycling.

Among the aforementioned challenges, preventing the shuttle of lithium polysulfides (LiPSs) has been attached great importance. In the past few years, to overcome this issue, numerous studies are mainly concentrated on the sulfur cathode [7,8]. Traditional carbon materials [9–14], metal organic framework (MOF) based materials [15,16], transition metal oxides [17] and sulfides [18] have been applied to improve the performance of the sulfur cathodes. However, the sulfur content of the cathodes is inevitably reduced by the addition of the considerable amount of the functional materials, decreasing the total energy density of Li-S battery. Meanwhile, even for the modified cathode, there is still nonnegligible sulfur loss into the electrolyte during the cycling, especially for the cathode with high sulfur loading,

* Corresponding authors.
E-mail addresses: xuxu@whut.edu.cn (X. Xu), mlq518@whut.edu.cn (L. Mai).

https://doi.org/10.1016/j.cej.2020.124979
Received 6 February 2020; Received in revised form 20 March 2020; Accepted 4 April 2020
Available online 10 April 2020

making the battery difficult to survive for a long time.

The separator is also an indispensable part of the battery to isolate the electrons and transport the ions between the two electrodes. For Li-S batteries, the requirement for an ideal separator is even higher than that in LIBs, ascribing to the existence of the soluble polysulfides. The most commonly used separators for Li-S batteries are monolayer and triple-layered polyolefin separators, which are commercialized for LIBs. This type of separator possesses a large number of micron/nano-sized pores, providing channels for the transport of lithium ions. However, at the same time, the polysulfides can also easily pass through the membrane to the lithium anode, leading to unfavorable side reactions. And these polyolefin separators have poor wettability to the ether-based electrolyte in Li-S batteries, which also affects their ability to contain electrolytes. Moreover, the mechanical properties and high temperature resistance of the polyolefin separators are poor, which may cause serious safety problems. In order to solve these problems in polypropylene separators, much efforts have been committed to modify the polyolefin separators or design a polysulfide interlayer between the separator and cathode [19–37]. For the purpose of tapping polysulfides, most modification layers were operated with relatively high mass loadings, decreasing the energy density of the whole batteries. And the modification materials of the separators will partially block the ion pathways and thus increase the impedance of the batteries. Moreover, the adhesion of the modification layer to the separator is usually weak, making it easily detach from the separator during cycling. Meanwhile, the modification still cannot solve the problems of the poor mechanical properties and high temperature resistance of polyolefin separator.

With unparalleled advantages in electrolyte absorption and ion transport, good mechanical properties and high temperature resistance performance, electrospun polymer nanofiber membranes have been widely considered as potential candidates for battery separators [38,39]. The commonly used electrospun materials include polyvinylidene fluoride (PVDF) [40,41], polyethylene terephthalate (PET) [42], polyacrylonitrile (PAN) [43]. However, since the polymer membranes do not have an adsorption effect on the polysulfides, when employed as separators for Li-S batteries, functional additives are usually adopted to trap polysulfides. Graphene oxide (GO) and reduced graphene oxide (rGO) have been widely used as polysulfides adsorbent materials due to the high surface area and the polar oxygen-containing groups [44]. Zhu et al. fabricated a double-layer rGO–PVDF/PVDF membrane [45], in which the rGO was introduced to ensure the fast transfer of Li-ions and block the shuttle of polysulfides. With the low content of rGO, the batteries showed an initial capacity of 1322 mA h g^{-1} at 0.2 C for the first cycle, but only 646 mAh g^{-1} was remained after 200 cycles. Recently, ammonium polyphosphate (APP) was introduced into the electrospun PAN nanofiber membrane to obtain a modified separator for adsorbing polysulfides [46], and a better electrochemical performance was obtained with this functional separator. However, the functional component APP is mostly wrapped inside the PAN nanofibers according to the characterizations, which seriously limited the efficiency of APP. Hence it is significant to improve the configuration of a composite separator by exposing the functional materials to the electrolyte.

2. Experimental section

All chemicals were used as received without purification. $Co(acac)_2$ (97%), N,N-dimethylformamide (DMF), PAN (Mw = 150000) were purchased from Macklin. 1,3-Dioxlane (DOL) (99.5%), 1,2-Dimethoxyethane (DME) (99.5%), $LiNO_3$(99.9%), Li_2S and sublimed sulfur power were purchased from Alfa Aesar. Graphene oxide suspension was synthesized by Hummer's method using natural flake graphite [47,48].

2.1. Preparation of $Co(acac)_2$-PAN/GO-PAN membrane

For the preparation of GO-PAN solution, 0.1 g GO was first dispersed in 10 mL DMF. PAN was then added to the GO-dispersed solution and kept stirring before forming a homogenous GO-PAN (PAN, 10 wt%) solution. The $Co(acac)_2$-PAN solution was prepared by dispersing 2 mmol $Co(acac)_2$ in 10 mL DMF via sonication. Then, 2 g PAN was added into the $Co(acac)_2$ solution sequentially with stirring at 70 °C overnight. GO-PAN membrane was prepared by electrospinning. GO-PAN solution was fed through the needle tip with a syringe pump at the feeding rate of 0.05 mm min^{-1} with a high positive voltage (12.0 kV), and the distance between the needle tip and the round collector was 15 cm. Then double-layer membrane was prepared by directly electrospinning the $Co(acac)_2$-PAN solution onto the as-prepared PAN-GO membrane. The thickness of the membrane was controlled around 135 ± 5 μm. The PAN/GO-PAN membrane was prepared with the same method without $Co(acac)_2$.

2.2. Preparation of the MOF-PAN/rGO-PAN membrane

A piece of the as-prepared $Co(acac)_2$-PAN/GO-PAN membrane (10 cm × 10 cm) and 2-Methylimidazole powders were treated at 150 °C under low-pressure condition for 8 h, obtaining MOF-PAN/rGO-PAN membrane. The obtained membrane was then pressed with a roller machine. And it was cut into a circular separator with a diameter of 1.9 cm. The PAN/GO-PAN nanofiber membrane was treated at a same condition to obtain PAN/rGO-PAN separator.

2.3. Preparation of the Li_2S_6 solution

Li_2S and S power was added to the liquid mixture of 1, 2-dimethoxyethane (DME) and 1, 3-dioxolane (DOL) (1:1 in volume) and homogenized by vigorous stirring at 70 °C for 48 h. The concentration of the prepared Li_2S_6 solution was 0.02 M.

2.4. Materials characterization

X-ray diffraction (XRD) characterization was performed to investigate the crystallographic information of samples using a D8 Advance X-ray diffractometer with a non-monochromated Cu Ka X-ray source (λ = 1.054056 Å). Scanning electron microscopic (SEM) images were collected by using a JEOL JSM-7100F at an acceleration voltage of 15 kV. Transmission electron microscopic (TEM) and high-resolution TEM (HRTEM) images were recorded with a Titan G2 60–300 with EDS image corrector. Differential scanning calorimetry (DSC) and thermogravimetric analysis (TGA) was performed using a Netzsch STA 449C simultaneous analyzer. X-ray photoelectron spectroscopy (XPS) measurements were conducted using a VG MultiLab 2000 instrument. The Dynamic contact angle measurements were conducted using an optical contact angle measuring and contour analysis system (Dataphysics DCA 35).

2.5. Electrochemical measurement

CR2025 type coin cells were assembled in an argon filled glovebox. And the contents of water and oxygen were both below 0.1 ppm. The mechanically pressed rGO-S samples with thickness around 100 μm were directly used as the cathode [49], and lithium foil was used as anode. The electrolyte was a solution of 1 M LiTFSI in (1:1) DEM and DOL, and $LiNO_3$ (1 wt%) was severed as an additive. The ratio of electrolyte to S is 20(μL):1(mg). The cycling tests were performed at low current density for initial few cycles. The Galvanostatic charge/discharge cycling was carried out in a CT 2001A multichannel battery testing system (Wuhan LAND Electronic Co, Ltd) with a potential range of 1.7–2.8 V vs. Li/Li^+. The cycle cyclic voltammetry (CV) curves and electrochemical impedance spectroscopy (EIS) tests (0.1 Hz–100 kHz,

5 mV) were conducted on an electrochemical workstation (Autolab PGSTAT302N).

The lithium ion transference number for different separators was determined with chronoamperometry by using electrochemical working station at a constant step potential of 10 mV. Each membrane was separately sandwiched between two lithium metal electrodes in a coin type cell (CR2025) and lithium ion transference number was calculated from the ratio of steady state current to initial state current according to the following equation:

$$t_{Li+} = Is/I_0$$

where t_{Li+} is transference number, while Is and I_0 represent the current at the steady state and initial state, respectively [43,50].

2.6. Theoretical calculation method

Density functional theory calculations were carried out by CASTEP module implemented in Accelrys Material Studio. The binding energies of ZIF-67 with Li_2S_n (n = 1, 2, 4, 6, 8) were computed to evaluate the immobilization effect of Li_2S_n inside ZIF-67. The Perdew-Burke-Ernzerhof (PBE) exchange–correlation functional was used, combining with the Grimme dispersion correction method. The energy convergence value of electronic optimization was 10^{-6} eV/atom, which was proceeded with the plane wave cutoff energy of 544.2 eV and the Γ-centered k-mesh of 1 × 1 × 1. For ionic optimization, the energy convergence threshold was 10^{-5} eV/atom and the max force was 0.03 eV/Å. The binding energy (E_b) is calculated abiding by the following equation:

$$E_b = E(ZIF{-}67\_Li_2S_n) - E(ZIF{-}67) - E(Li_2S_n)$$

where E refers to the energy of corresponding material in front bracket.

3. Results and discussion

Herein, a finely crafted double-layered MOF-PAN/rGO-PAN nanofiber membrane is prepared through electrospinning and the following low pressure chemical vapor deposition (LPCVD) of MOFs. The membrane as the separator for Li-S batteries achieves several vital improvements, whose structural schematic is shown in Fig. 1a. Firstly, compared with the liquid-phase method, the LPCVD method for *in situ* growing the MOFs particles maintains the good mechanical property and thermal stability of the PAN nanofiber network, and the MOF particles are closely attached on the nanofibers so that the integrity of the membrane can be well kept during cycling [51]. Secondly, the PAN network has good electrolyte wettability and abundant pores to accommodate the electrolyte to ensure the high ion conductivity, and its large surface area can provide a lot of polysulfide adsorption sites to impede its diffusion through the separator. Thirdly, the exposed MOF particles can maximize the utilization for trapping polysulfides through chemisorption, which shows obvious advantages over the separators with functional component embedded inside the fibers. Moreover, the rGO-PAN layer can temporize the transport of the flux of Li-ions to the anode surface, which can restrain the structural change of Li anode.

The MOF-PAN/rGO-PAN nanofiber membrane was simply synthesized by two steps. First, the double-layered $Co(acac)_2$-PAN/GO-PAN nanofiber membrane was prepared by electrospinning, in which $Co(acac)_2$ acted as the cobalt source for the following synthesis of MOF particles. The smooth surface of $Co(acac)_2$-PAN nanofibers with diameter of 200 nm can be distinctly observed in the SEM image (Fig. S1a), which shows no difference with pure PAN membrane (Fig. S1b). And the elemental mappings of $Co(acac)_2$-PAN nanofibers show the uniform distributions of elements Co, C, N, and O (Fig. S2).

After the *in situ* growth of MOFs, the structure of the double-layered MOF-PAN/rGO-PAN membrane is completely retained, which shows obvious advantage of LPCVD over the hydrothermal method for the synthesis of MOFs. A large number of nano-sized MOF particles are evenly distributed in the network and closely attached on the surface of the nanofibers (Fig. 1b, c).

Compared with PP separator, the three-dimensional porous nanofiber network with high specific surface area possesses more space to accommodate electrolyte, which can compensate the electrolyte consumed during cycling. And the areal mass of the functional separator is only 0.5 mg cm^{-2}, which is smaller than that of commercial PP separator (1.4 mg cm^{-2}). The rGO-PAN layer shows a rough surface with wrinkled rGO sheets randomly distributed in the network (Fig. S3a,b). The total thickness of MOF-PAN/rGO-PAN double-layer membrane is about 135 μm (Fig. S3c), and there is no obvious boundary between the two layers, showing good integrity of the membrane. The two layers can only be distinguished by the elemental mappings (Fig. S4). The TEM image further validates the formation of MOF on the surface of PAN nanofibers (Fig. 1d). The MOF particles *in situ* grew on the nanofibers and the adhesive force is extremely strong (Fig. 1e). The lattice fringes of the MOF particle can be clearly observed under HRTEM image (Fig. 1f). Moreover, a very thin MOF layer with the thickness of several nanometers is also found on the surface of the PAN nanofiber (Fig. 1g). The XRD pattern of the membrane exhibits clear characteristic peaks of ZIF-67 (Fig. S5a). FTIR was also carried out to further analyze the chemical structure and functional groups of the membranes (Fig. S5b). Compared to PAN and rGO-PAN membranes, MOF-PAN membrane display a typical peak at 750 cm^{-1}, further proving the successful synthesis of ZIF-67 by LPCVD [52,53].

The good wettability of the double-layered MOF-PAN/rGO-PAN membrane was confirmed by dynamic contact angle measurements. The MOF-PAN/rGO-PAN membrane was immediately wetted when the electrolyte was dropped on (Fig. 2a).

In contrast, the initial contact angle of PP separator was about 45°, which remained almost unchanged for 30 s (Fig. 2b). The thermal stabilities of different membranes were first studied by DSC. As show in Fig. 2c, the PP separator shows an obvious endothermic peak around 168 °C, which is due to the melting of PP [54].

However, even the temperature increases to 210 °C, no peaks are observed for the MOF-PAN/rGO-PAN membrane. The TGA demonstrates that the thermal degradation of MOF-PAN/rGO-PAN membrane begins at ~300 °C (Fig. 2d), which illustrates that its thermal stability is much better than that of PP separator. In order to directly show the good thermal stability of PAN-based separators, the digital pictures of PP, PAN, PAN/rGO-PAN, MOF-PAN/rGO-PAN before and after thermal treatment at 100 °C are displayed in Fig. 2e and f, respectively. After treated for 1 h, it can be clearly observed that the PP separator is rolled up, while the PAN-based membranes do not appear any change in color or shape.

The self-discharge effect of Li-S batteries is one of the reasons that affect its commercialization. So we first tested the self-discharge performance of Li-S cells, using MOF-PAN/rGO-PAN membrane and PP as the separators, respectively. The cell with MOF-PAN/rGO-PAN separator only shows a slight voltage drop in the initial few hours, and then stabilizes at 2.36 V even after 72 h (Fig. 3a), while the cell with PP separator shows a seriously continuous voltage drop. The transference number of lithium ion is an important factor for the electrochemical performance of a battery. Symmetrical cells were assembled with different separators to compare the transference numbers of lithium ion. With a constant potential of 10 mV, the different current-time (i-t) curves were obtained (Fig. 3b–d), and the transference number of lithium ion defined by the ratio of the steady current to the initial current were calculated. The results show that the lithium ion transference number of MOF-PAN/rGO-PAN separator is 0.81, higher than 0.78 of PAN/rGO-PAN and 0.68 of PP separator, which may be attributed to the interaction of the metal ions in MOF with the anion in the electrolyte.

The EIS test of Li-S battery with different separators is shown in Fig. S6 in the Supporting Information. It is obvious that the resistance (Rct) of the cell with MOF-PAN/rGO-PAN separator has a smaller charge

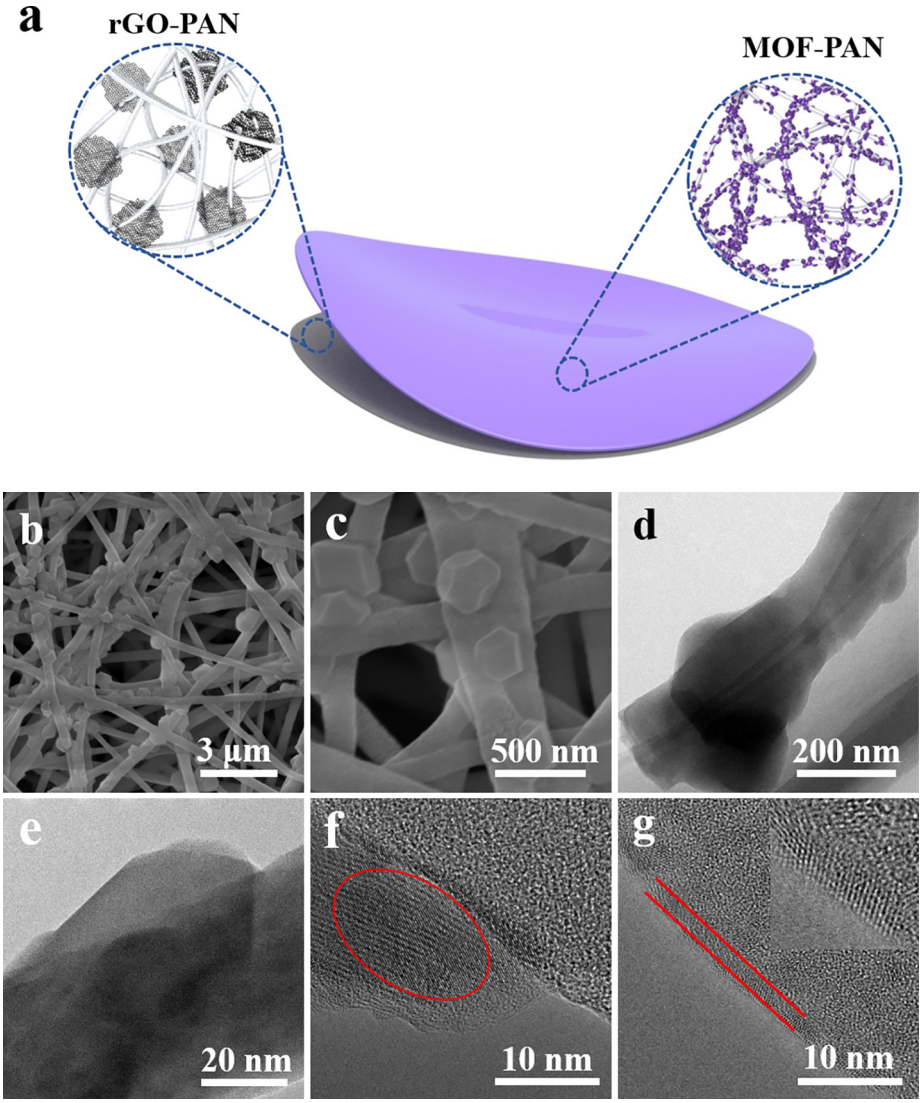

Fig. 1. (a) Schematic of the multifunctional electrospun MOF-PAN/rGO-PAN separator and PP separator for Li-S batteries; (b-g) morphological characterization of MOF-PAN/rGO-PAN, (b, c) SEM images; (d, e) TEM images and (f, g) HRTEM images. The illustration of g is an enlargement of the red part. (For interpretation of the references to color in this figure legend, the reader is referred to the web version of this article.)

transfer resistance (52 Ω) than that of the cell with PAN/rGO-PAN (58 Ω) and PP separator (105 Ω), which is also due to the good ionic conductivity of PAN and the positive role of MOF.

The electrochemical performance of Li-S batteries with MOF-PAN/rGO-PAN separators were evaluated by assembling the coin cells using the freestanding rGO/sulfur composite as the cathode. The areal sulfur loading of cathode for routine electrochemical performance test is 2.6 mg cm^{-2}. The initial three CV curves of the battery show no obvious changes of the peak positions, indicating the good reversibility of the batteries (Fig. S7a). In the discharge stage, two typical cathodic peaks located at 2.25 and 2.03 V can be observed, which are due to the formation of soluble LiPSs and then to the insoluble discharge products Li_2S_2/Li_2S, respectively. The anodic peak around 2.43 V belongs to electrochemical transformation of Li_2S_2/Li_2S to sulfur. In contrast, CV curves of the batteries with PP and PAN/rGO-PAN separators display obvious polarization, indicating the sluggish reaction kinetics (Fig. S7b).

The rate performance of the battery with MOF-PAN/rGO-PAN was further studied (Fig. 4a). Reversible capacities of 1302, 1126, 909, 745, 485 mAh g^{-1} are achieved at 0.5 C, 1 C, 2 C, 3 C and 5 C, respectively. When the current density switching back to 0.5 C, an average capacity of 1270 mAh g^{-1} is recovered. Even at high current densities, there are still two distinct voltage plateaus for each discharge curve, which reflects the good ionic conductivity and low impedance of MOF-PAN/rGO-PAN separator (Fig. S8). Li-S cells with PP and PAN/rGO-PAN separators show apparently poorer rate performance, especially at high rates. The initial galvanostatic charge/discharge curves of batteries assembled with MOF-PAN/rGO-PAN and PP separators at 0.5 C are compared in Fig. 4b. The discharge plateaus of the cells with MOF-PAN/rGO-PAN separator (η = 0.22 V) are flatter than the cells with PP separator (η = 0.32 V), indicating the lower polarization.

The cycling performances of the batteries with MOF-PAN/rGO-PAN, PAN/rGO-PAN, PP separators are systematically investigated. At 1 C, the cell with MOF-PAN/rGO-PAN separator shows a high initial discharge capacity of 1116 mAh g^{-1}, and it can maintain 925 mAh g^{-1} after 100 cycles with the capacity retention of 83%. On the other hand, the cells with PAN/rGO-PAN and PP show fast capacity fading, and the capacities of only 638 and 487 mAh g^{-1} remain after 100 cycles, respectively (Fig. 4c).

To further confirm the long-term stability of MOF-PAN/rGO-PAN separator, the battery was tested at 5 C for 600 cycles (Fig. 4d). After the activation at a low rate, an initial discharge capacity of 441 mAh g^{-1} at 5 C was obtained, and 356 mAh g^{-1} was remained after 600 cycles. The capacity retention is 81% and the corresponding

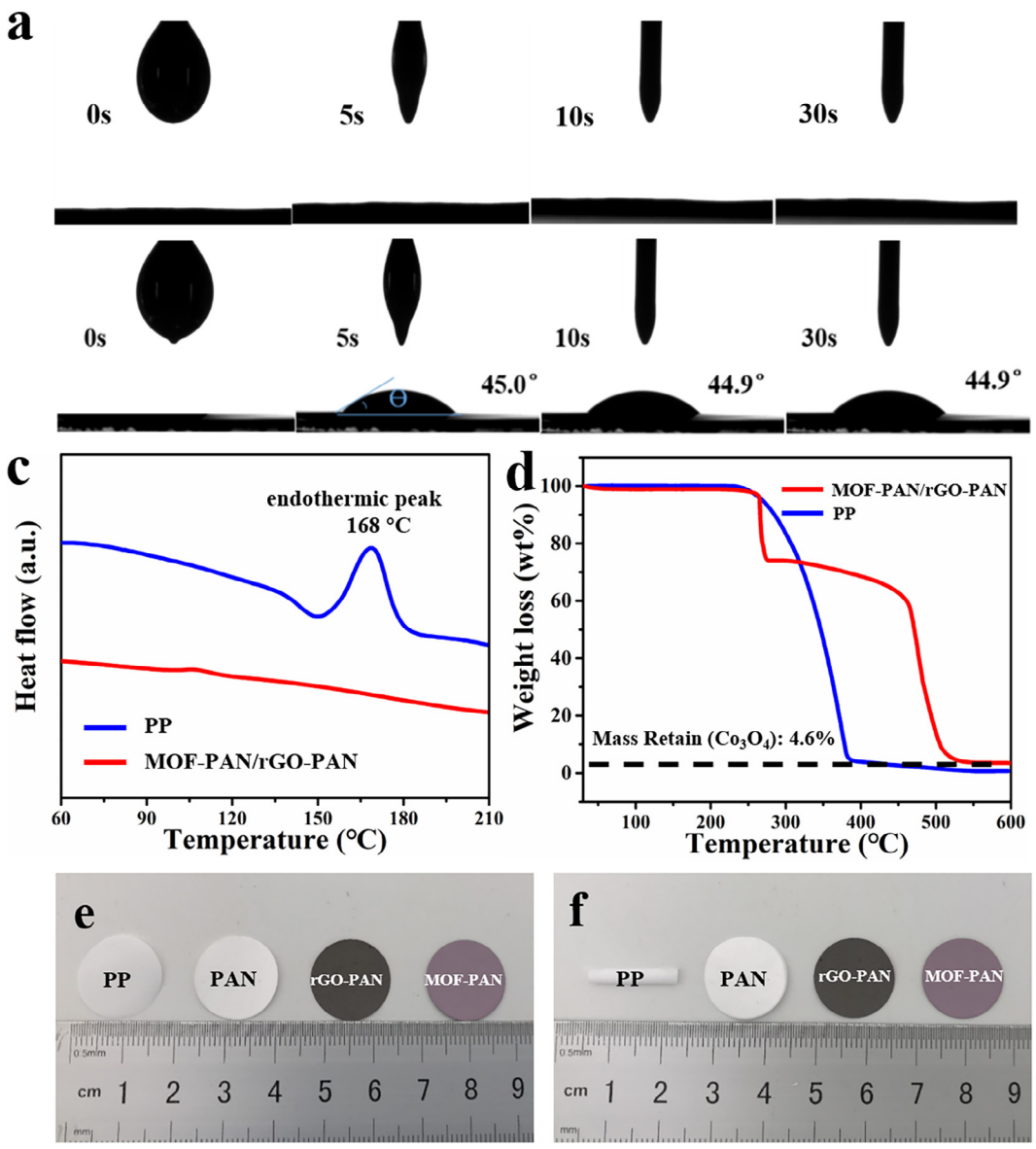

Fig. 2. Dynamic contact angle measurements with electrolyte for (a) MOF-PAN/rGO-PAN membrane; (b) PP separator; (c, d) DSC and TGA curves of PP separator and MOF-PAN/rGO-PAN membrane; (e, f) the optical pictures of PP, PAN, PAN/rGO-PAN, MOF-PAN/rGO-PAN membranes before and after thermal treatment at 100 °C.

capacity fading rate is only 0.03% per cycle. For the purpose of the practical application, Li-S batteries must have a sulfur loading higher than 5 mg cm^{-2} [55,56]. However, with a high loading of insulating sulfur, much severe shuttle effect occurs simultaneously, which put forward higher requirements for the separator. As shown in Fig. 4e, when the areal sulfur loading increasing to 7.7 mg cm^2, the cells with MOF-PAN/rGO-PAN separator showed an initial capacity of 1102 mAh g^{-1} (8.5 mAh cm^{-2}) at 0.2 C, and remained 1008 mAh g^{-1} (7.8 mAh cm^{-2}) after 50 cycles, which illustrates that this functional separator can also effectively inhibit the LiPSs shuttle effect even at a high areal sulfur loading. The corresponding areal capacities are higher than the commercial LIBs (4.0 mAh cm^{-2}).

In order to explore the effect of different separators on polysulfide permeation, a visual observation experiment was carried out with a double-L device, and Li_2S_6 solution and blank electrolyte were separated by the separator. For PP (Fig. 5a) or PAN/rGO-PAN (Fig. 5b) separator, the Li_2S_6 solution gradually diffused through the separator, and the penetration became more and more serious as time going on. In contrast, for the MOF-PAN/rGO-PAN separator, even after 24 h, almost no polysulfide penetrated into the blank electrolyte (Fig. 5c). To further reveal the LiPSs adsorption mechanism of the MOF-PAN layer, the density functional theory (DFT) calculation is introduced to this work. The molecular skeletons of ZIF-67 in different sides are shown in Fig. 5d. The strong interactions between LiPSs and ZIF-67 were confirmed by DFT calculations, which is due to the bondings of Co-S, N-S, and O-S. The binding energies (E_b) of Li_2S, Li_2S_2, Li_2S_4, Li_2S_6, Li_2S_8 and S_8 on ZIF-67 are 3.29 eV, 2.74 eV, 3.20 eV, 3.25 eV, 3.34 eV, and 3.15 eV, respectively (Fig. 5e). This result further confirms the strong adsorption of MOF to polysulfides and reveals the reason for the improvement of Li-S battery performance.

4. Conclusion

In conclusion, we designed and prepared a double-layered MOF-PAN/rGO-PAN nanofiber membrane by electrospinning and the following LPCVD methods. Besides the intrinsic advantages of PAN-based membrane as a separator for Li-S batteries, such as good mechanical property, thermal stability and high electrolyte uptake, the MOF

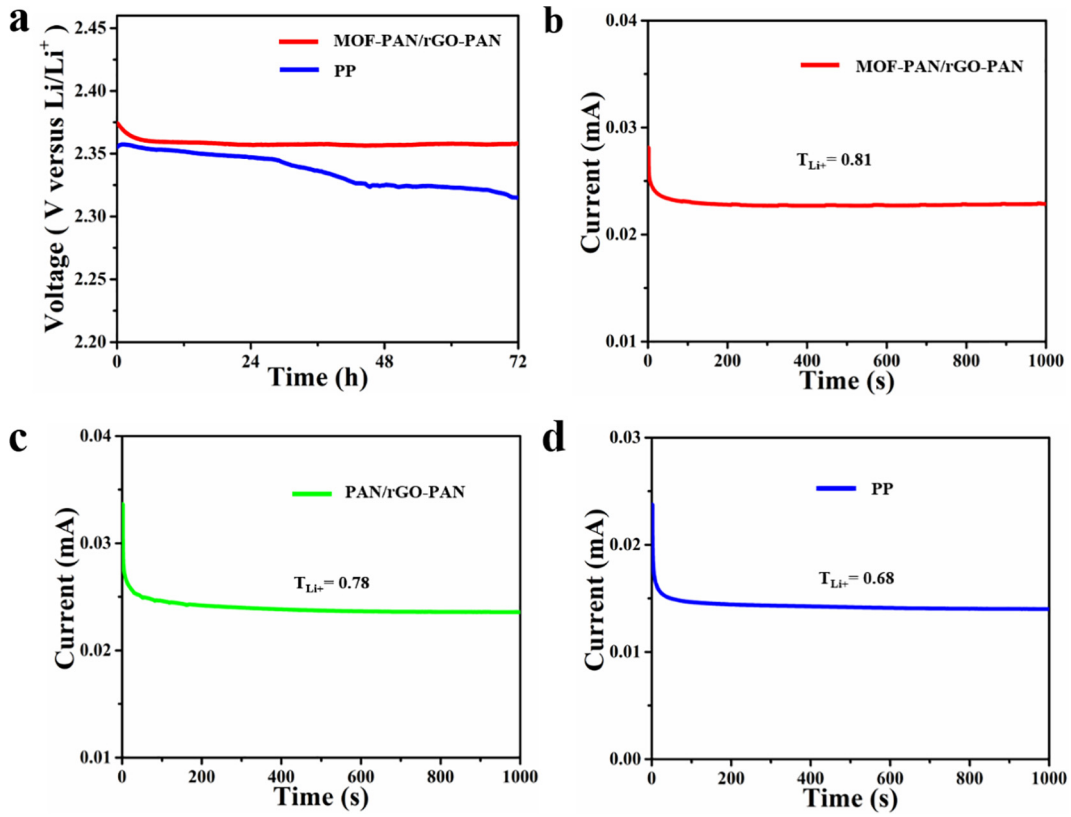

Fig. 3. (a) The open circuit voltage curves of Li-S batteries with different separators; (b-d) lithium ion transference number tests of MOF-PAN/rGO-PAN, PAN/rGO-PAN, and PP separators.

practices grown on the nanofibers can strongly adsorb the polysulfides, which effectively inhibits the shuttle effect and improves the cycling stability. The MOF-PAN/rGO-PAN separator shows negligible self-discharge and a high lithium ion transference number of 0.81. With this novel functional separator, the Li-S batteries can provide a high initial capacity of 1302 mAh g^{-1} at 0.5 C. At a high rate of 5 C, the capacity decay rate is only 0.03% per cycle over 600 cycles. More importantly, even with a high sulfur loading of 7.7 mg cm^{-2}, the Li-S battery delivered a high areal capacity of 7.8 mAh cm^{-2} after 50 cycles. The DFT calculation further confirmed that the MOF-PAN layer attach great

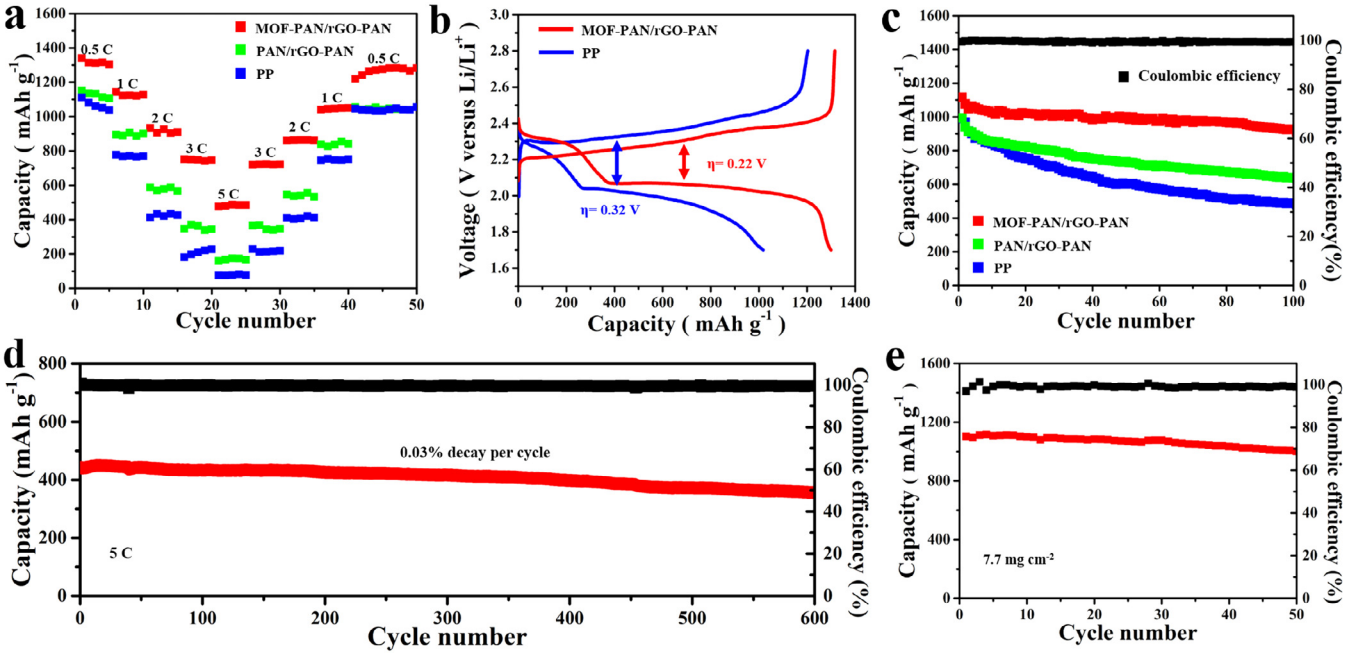

Fig. 4. (a) The rate performance of Li-S batteries using different separators; (b) galvanostatic charging/discharging performance of Li-S batteries with different separators at 0.5 C; (c) the cycling performances of Li-S cells with different separators at 1 C for 100 cycles; (d) the long-term cycling performance of Li-S cell with MOF-PAN/rGO-PAN separator at 5 C for 600 cycles; (e) the high loading test of Li-S cells with MOF-PAN/rGO-PAN separator.

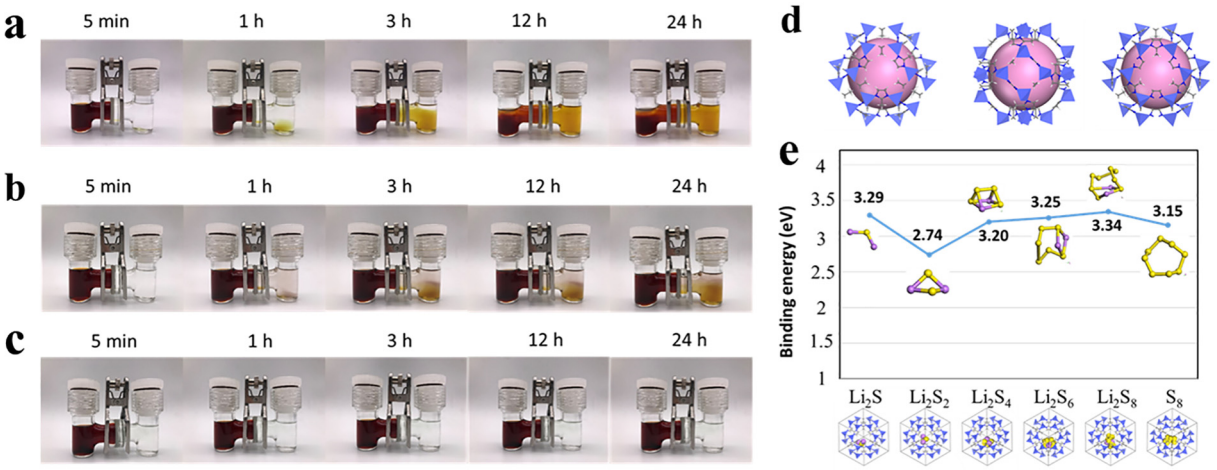

Fig. 5. Permeation experiments with a double-L device for (a) PP; (b) PAN/rGO-PAN and (c) MOF-PAN/rGO-PAN separators; (d) DFT molecular skeletons of ZIF-67 in different sides; (e) optimized configurations for the binding of Li_2S_n and S_8 to ZIF-67.

importance in improving the electrochemical performance of the Li-S batteries. Therefore, the MOF-PAN/rGO-PAN nanofiber separator shows bright prospect in achieving high-performance Li-S batteries.

Declaration of Competing Interest

The authors declare that they have no known competing financial interests or personal relationships that could have appeared to influence the work reported in this paper.

Acknowledgements

This work was supported by the National Natural Science Foundation of China (51702247, 51832004, 51521001), the National Key Research and Development Program of China (2016YFA0202603, 2018YFB0104200), the Programme of Introducing Talents of Discipline to Universities (B17034), the Yellow Crane Talent (Science & Technology) Program of Wuhan City and the Fundamental Research Funds for the Central Universities (WUT: 2019III174).

Appendix A. Supplementary data

Supplementary data to this article can be found online at https://doi.org/10.1016/j.cej.2020.124979.

References

[1] J. Tarascon, M. Armand, Nature 414 (2001) 359–367.
[2] J. Owen, Chem. Soc. Rev. 26 (1997) 259–267.
[3] X. Ji, K. Lee, L. Nazar, Nat. Mater. 8 (2009) 500–506.
[4] P. Bruce, S. Freunberger, L. Hardwick, J. Tarascon, Nat. Mater. 11 (2012) 19–29.
[5] A. Manthiram, Y. Fu, Y. Su, Acc. Chem. Res. 46 (2013) 1125–1134.
[6] T. Chen, W. Kong, P. Zhao, H. Lin, Y. Hu, R. Chen, W. Yan, Z. Jin, Chem. Mater. 31 (2019) 7565–7573.
[7] Z. Li, Q. He, X. Xu, Y. Zhao, X. Liu, C. Zhou, D. Ai, L. Xia, L. Mai, Adv. Mater. 30 (2018) 1804089.
[8] L. Ma, W. Zhang, L. Wang, Y. Hu, G. Zhu, Y. Wang, R. Chen, T. Chen, Z. Tie, J. Liu, Z. Jin, ACS Nano 12 (2018) 4868–4876.
[9] Y. Chen, S. Choi, D. Su, X. Gao, G. Wang, Nano Energy 47 (2018) 331–339.
[10] L. Lin, F. Pei, J. Peng, A. Fu, J. Cui, X. Fang, N. Zheng, Nano Energy 54 (2018) 50–58.
[11] D. Su, M. Cortie, G. Wang, Adv. Energy Mater. 7 (2017) 1602014.
[12] X. Liang, Y. Rangom, C. Kwok, Q. Pang, L. Nazar, Adv. Energy Mater. 29 (2016) 1603040.
[13] F. Wu, E. Zhao, D. Gordon, Y. Xiao, C. Hu, G. Yushin, Adv. Mater. 28 (2016) 6365–6371.
[14] L. Ma, G. Zhu, W. Zhang, P. Zhao, Y. Hu, Y. Wang, L. Wang, R. Wang, T. Chen, Z. Tie, J. Liu, Z. Jin, Nano Res. 11 (2018) 6436–6446.
[15] J. Zhou, R. Li, X. Fan, Y. Chen, R.D. Han, W. Li, J. Zheng, B. Wang, X. Li, Energy Environ. Sci. 7 (2014) 2715.
[16] T. Pan, Z. Li, Q. He, X. Xu, L. He, J. Meng, C. Zhou, Y. Zhao, L. Mai, Energy Storage Mater. 23 (2019) 55–61.
[17] X. Wang, T. Gao, X. Fan, F. Han, Y. Wu, Z. Zhang, J. Li, C. Wang, Adv. Funct. Mater. 26 (2016) 7164–7169.
[18] X. Liu, J. Huang, Q. Zhang, L. Mai, Adv. Mater. 29 (2017) 1601759.
[19] L. Ma, H. Lin, W. Zhang, P. Zhao, G. Zhu, Y. Hu, R. Chen, Z. Tie, J. Liu, Z. Jin, Nano Lett. 18 (2018) 7949–7954.
[20] S. Chung, A. Manthiram, Adv. Mater. 26 (2014) 1360–1365.
[21] T. Chen, Z. Zhang, B. Cheng, R. Chen, Y. Hu, L. Ma, G. Zhu, J. Liu, Z. Jin, J. Am. Chem. Soc. 139 (2017) 12710–12715.
[22] G. Zhou, L. Li, D. Wang, X. Shan, S. Pei, F. Li, H. Cheng, Adv. Mater. 27 (2015) 641–647.
[23] H. Peng, D. Wang, J. Huang, X. Cheng, Z. Yuan, F. Wei, Q. Zhang, Adv. Sci. 3 (2016) 1500268.
[24] L. Shi, F. Zeng, X. Cheng, K. Lam, W. Wang, A. Wang, Z. Jin, F. Wu, Y. Yang, Chem. Eng. J. 334 (2018) 305–312.
[25] T. Zhuang, J. Huang, H. Peng, L. He, X. Cheng, C. Chen, Q. Zhang, Small 12 (2016) 381–389.
[26] X. Song, S. Wang, G. Chen, T. Gao, Y. Bao, L. Ding, H. Wang, Chem. Eng. J. 333 (2018) 564–571.
[27] Z. Huang, M. Yang, J. Qi, L. Lei, Q. Du, L. Bai, H. Fu, X. Yang, R. Liu, T. Masese, H. Zhang, T. Ma, Chem. Eng. J. 387 (2020) 124080.
[28] P. Kim, J. Seo, K. Fu, J. Choi, Z. Liu, J. Kwon, L. Hu, U. Paik, NPG Asia Mater. 9 (2017) e375.
[29] Y. Liu, Y. Qiao, Y. Zhang, Z. Yang, T. Gao, D. Kirsch, B. Liu, J. Song, B. Yang, L. Hu, Energy Storage Mater. 12 (2018) 197–203.
[30] L. Ma, R. Chen, G. Zhu, Y. Hu, Y. Wang, T. Chen, J. Liu, Z. Jin, ACS Nano 11 (2017) 7274–7283.
[31] C. Song, G. Li, Y. Yang, X. Hong, S. Huang, Q. Zheng, L. Si, M. Zhang, Y. Cai, Chem. Eng. J. 381 (2020) 122701.
[32] L. Ma, H. Yuan, W. Zhang, G. Zhu, Y. Wang, Y. Hu, P. Zhao, R. Chen, T. Chen, J. Liu, Z. Hu, Z. Jin, Nano Lett. 17 (2017) 7839–7846.
[33] T. Lei, W. Chen, W. Lv, J. Huang, J. Zhu, J. Chu, C. Yan, C. Wu, Y. Yan, W.D. He, J. Xiong, Y. Li, C. Yan, J. Goodenough, X. Duan, Joule 2 (2018) 2091–2104.
[34] J. He, Y. Chen, A. Manthiram, Energy Environ. Sci. 11 (2018) 2560–2568.
[35] L. Ma, R. Chen, Y. Hu, W. Zhang, G. Zhu, P. Zhao, T. Chen, C. Wang, W. Yan, Y. Wang, L. Wang, Z. Tie, J. Liu, Z. Jin, Energy Storage Mater. 14 (2018) 258–266.
[36] Y. Yang, S. Wang, L. Zhang, Y. Deng, H. Xu, X. Qin, G. Chen, Chem. Eng. J. 369 (2019) 77–86.
[37] G. Jiang, N. Zheng, X. Chen, G. Ding, Y. Li, F. Sun, Y. Li, Chem. Eng. J. 373 (2019) 1309–1318.
[38] H. Lee, M. Yanilmaz, O. Toprakci, K. Fu, X. Zhang, Energy Environ. Sci. 7 (2014) 3857–3886.
[39] T. Chen, W. Kong, Z. Zhang, L. Wang, Y. Hu, G. Zhu, R. Chen, L. Ma, W. Yan, Y. Wang, J. Liu, Z. Jin, Nano Energy 54 (2018) 17–25.
[40] M. Yanilmaz, Y. Lu, M. Dirican, K. Fu, X. Zhang, J. Membr. Sci. 456 (2014) 57–65.
[41] C. Zhu, T. Nagaishi, J. Shi, H. Lee, P. Wong, J. Sui, K. Hyodo, I. Kim, ACS Appl. Mater. Interfaces 9 (2017) 26400–26406.
[42] J. Hao, G. Lei, Z. Li, L. Wu, Q. Xiao, L. Wang, J. Membr. Sci. 428 (2013) 11–16.
[43] J. Zhu, C. Chen, Y. Lu, J. Zang, M. Jiang, D. Kim, X. Zhang, Carbon 101 (2016) 272–280.
[44] X. Liu, K. Song, C. Lu, Y.T. Huang, X. Duan, S. Li, Y. Ding, J. Membr. Sci. 555 (2018) 1–6.
[45] P. Zhu, J.D. Zhu, J. Zang, C. Chen, Y. Lu, M. Jiang, C. Yan, M. Dirican, R. Selvan, X. Zhang, J. Mater. Chem. A 5 (2017) 15096–15104.
[46] T. Lei, W. Chen, Y. Hu, W. Lv, X. Lv, Y. Yan, J. Huang, Y. Jiao, J. Chu, C. Yan, C. Wu, Q. Li, W. He, J. Xiong, Adv. Energy Mater. 8 (2018) 1802441.
[47] W. Hummers, R. Offeman, J. Am. Chem. Soc. 80 (1958) 1339.
[48] Y. Xu, L. Zhao, H. Bai, W. Hong, C. Li, G. Shi, J. Am. Chem. Soc. 131 (2009)

13490–13497.
[49] B. Papandrea, X. Xu, Y. Xu, C. Chen, Z. Lin, G. Wang, Y. Luo, M. Liu, Y. Huang, L. Mai, X. Duan, Nano Res. 9 (2016) 240–248.
[50] Y. Zhu, F. Wang, L. Liu, S. Xiao, Y. Yang, Y. Wu, Sci. Rep. 6 (2016) 38704.
[51] C. Zhang, L. Shen, J. Shen, F. Liu, G. Chen, R. Tao, S. Ma, Y. Peng, Y. Lu, Adv. Mater. 31 (2019) 1808338.
[52] J. Meng, X. Liu, J. Li, Q. Li, C. Zhao, L. Xu, X. Wang, F. Liu, W. Yang, X. Xu, Z.A. Liu, C. Niu, L. Mai, Nano Lett. 17 (2017) 7773–7781.
[53] W. Zhang, X. Jiang, X. Wang, Y. Kaneti, Y. Chen, J. Liu, J. Jiang, Y. Yamauchi, M. Hu, Angew. Chem. Int. Ed. 56 (2017) 8435–8440.
[54] Y. Miao, G. Zhu, H. Hou, Y. Xia, T. Liu, J. Power Sources 226 (2013) 82–86.
[55] C. Barchasz, F. Molton, C. Duboc, J. Lepretre, S. Patoux, F. Alloin, Anal. Chem. 84 (2012) 3973–3980.
[56] Y. Yin, S. Xin, Y. Guo, L. Wan, Angew. Chem. Int. Ed. 52 (2013) 13186–13200.